Pore-scale analysis of effects of electrode morphology and electrolyte flow conditions on performance of vanadium redox flow batteries

Gang Qiu [a], C.R. Dennison [b], K.W. Knehr [b], E.C. Kumbur [b], Ying Sun [a],*

[a] Complex Fluids and Multiphase Transport Laboratory, Department of Mechanical Engineering and Mechanics, Drexel University, Philadelphia, PA 19104, USA
[b] Electrochemical Energy Systems Laboratory, Department of Mechanical Engineering and Mechanics, Drexel University, Philadelphia, PA 19104, USA

HIGHLIGHTS

► We perform pore-scale simulations for different XCT-reconstructed electrode morphologies.
► We predict cell performance for different flow rates.
► Cell voltage saturates at high flow rates when concentration approaches uniformity.
► Fuel starvation is found to have a negative impact on cell voltage.
► We report statistical distributions of local parameters across the 3D porous electrode.
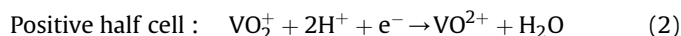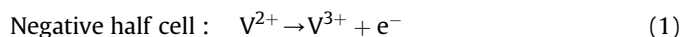
ARTICLE INFO

ABSTRACT

A 3D pore-scale transport resolved model is used to study the performance characteristics of a vanadium redox flow battery (VRFB) with various electrode morphologies under different operating conditions. Three electrode structures are reconstructed from X-ray computed tomography (XCT) images of porous carbon felt electrode materials. The local vanadium concentration, overpotential, current density and overall cell voltage for the positive half cell are examined. The results indicate that the cell voltage increases with increasing electrolyte flow rate due to decreasing concentration gradients of vanadium species within the porous electrode. However, the marginal gain in cell voltage diminishes once the concentration field approaches uniformity under convection-dominated mass transport conditions at sufficiently high electrolyte flow rates. The model also predicts that electrode structures with low porosity (high surface area) result in more uniform and lower absolute current density and overpotential fields at the expense of increased pressure drop. Finally, poor cell performance is observed for simulations operated at low electrolyte flow rates and low states of charge due to the fuel starvation (i.e., insufficient amount of reactant in the cell).

1. Introduction

The vanadium redox flow battery (VRFB) is considered a high-capacity energy storage technology used for storing energy from intermittent energy sources such as wind and solar [1–3]. At its core, the VRFB is a rechargeable battery that consists of two porous electrodes composed of carbon fibers that form an electrically conductive fibrous network separated by an ion exchange membrane (shown in Fig. 1). Vanadium-based electrolytes are circulated from external storage tanks through the porous electrodes, where electrochemical reactions occur on the surface of the electrode fibers. The vanadium species are dissolved in a sulphuric acid (H_2SO_4) solution where V^{3+} and V^{2+} ions are present in the negative electrolyte, and VO_2^+ and VO^{2+} (also known as V^{5+} and V^{4+}, respectively) ions are present in the positive electrolyte. During the discharging cycle, the following reactions take place at the surface of the carbon fibers:

Negative half cell : $\quad V^{2+} \rightarrow V^{3+} + e^-$ (1)

Positive half cell : $\quad VO_2^+ + 2H^+ + e^- \rightarrow VO^{2+} + H_2O$ (2)

The open circuit voltage (OCV) for reaction (1) is $E^{0,-} = -0.255$ V [4] and that for reaction (2) is $E^{0,+} = 0.991$ V [5] based on the Gibbs free energy, leading to a theoretical standard cell OCV of 1.246 V at a temperature $T = 298K$. Here, the superscripts $-$ and $+$ denote the negative and positive half-cell reactions, respectively.

* Corresponding author. Tel.: +1 215 895 1373; fax: +1 215 895 1478.
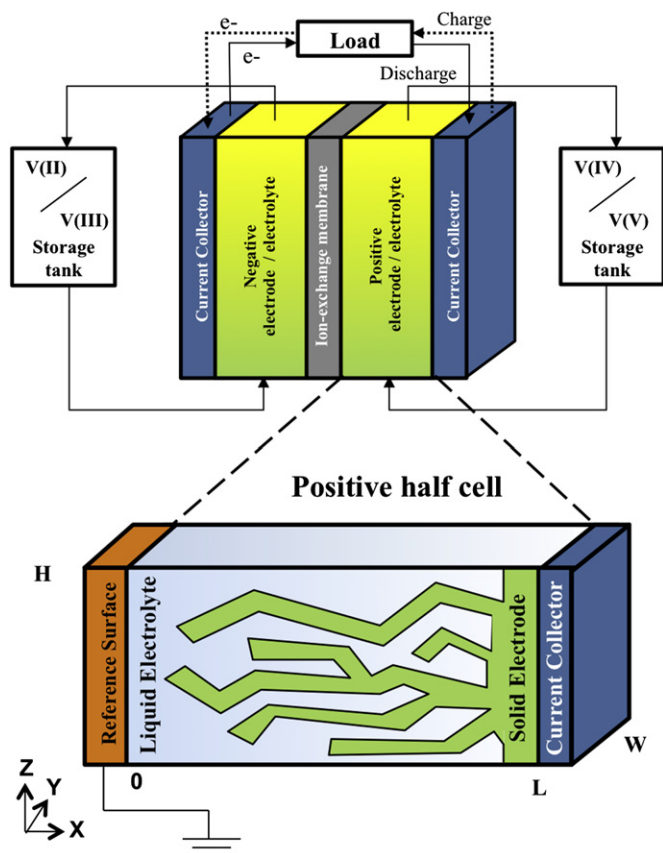E-mail addresses: ysun@coe.drexel.edu, ysunbu@gmail.com (Y. Sun).

Fig. 1. Schematic of the positive half cell of a vanadium redox flow battery.

The main advantage of VRFBs is that power generation and energy storage are decoupled, such that the energy storage capacity is determined by the size of the electrolyte tanks, whereas the power rating is dictated by the size and the number of redox cells [6]. However, transport losses in the electrode and low electrolyte utilization, among other losses, significantly affect the performance of VRFBs. During VRFB operations, both electrode microstructures (e.g., active surface area and porosity) and electrolyte flow conditions play important roles in determining the effectiveness of electrolyte transport inside a VRFB [7]. Experimental identification of optimal electrode microstructures and electrolyte flow configurations for VRFBs is very challenging and expensive. The widespread availability of supercomputers has made the use of advanced numerical modeling a valuable tool in assisting the design of VRFBs.

To serve this purpose, the authors have recently developed a pore-scale resolved transport model [8] for the VRFB where the porous electrode and electrolyte phases are distinctly separated and the electrolyte flow, species/charge transport, and electrochemistry are coupled and solved with pore-scale resolution. The greatest benefit of this pore-scale model is its capability of capturing the exact electrode morphology and electrolyte flow conditions and how these parameters affect the overall cell performance. As opposed to volumetric models [9–15] where the electrode/electrolyte domain is treated as a single continuum, the pore-scale resolved model does not rely on approximations of the electrode microstructure and hence offers a more accurate and detailed understanding of the coupled electrolyte flow, species/charge transport phenomena, and electrochemical reactions occurring locally within a VRFB. As such, the pore-scale model

enables investigation of key structurally dependent parameters that affect the electrolyte flow and utilization, thereby allowing for the characterization of the cell voltage parametrically for different electrode structures (e.g., size and orientation of the fibers, size/distribution of pores) and different operating conditions (e.g., flow rates, electrolyte concentration).

In this paper, the pore-scale model developed by the authors [8] is used to investigate the effects of electrode structural properties and electrolyte flow conditions on the electrolyte utilization and performance characteristics of VRFBs. A 3D, isothermal, positive half cell is used in the simulation, where the electrode geometry is based on an X-ray computed tomography (XCT) reconstructed porous carbon felt electrode material. The local and averaged vanadium concentration, overpotential, current density and cell voltage are reported for different electrode morphologies (e.g., active surface area and porosity), inlet state-of-charge (SOC), and flow rates.

The remainder of this paper is organized as follows. Section 2 describes the XCT reconstructed electrode geometry, model assumptions and equations, and the numerical implementation of the pore-scale resolved model. The verification of the half-cell model is shown in Section 3. Results are then presented and discussed in Section 4. Section 5 summarizes conclusions and recommendations for further study.

2. Methodology

2.1. XCT-reconstructed electrode geometry

For this study, a sample of Electrolytica GFS6-3 mm carbon felt (typically used in VRFBs) is imaged using a SkyScan 1172 X-ray tomograph. A virtual volume of the porous electrode medium is then reconstructed from the segmented tomograms. The 3D geometry is finally analyzed for key structural metrics such as porosity, specific surface area, pore and fiber sizes, and phase connectivity. A thorough discussion of this methodology is provided in Qiu et al. [8].

Fig. 2 shows three different electrode structures that were reconstructed from XCT. The geometric parameters corresponding to these structures are given in Table 1. The increased fiber density structures are attained by compressing the physical electrode medium, a phenomenon that occurs during the assembly of actual VRFB cells. This increase in fiber density also results in lower porosities and higher specific surface area. The structure of Fig. 2(a) is from an uncompressed sample of electrode and optimally matched the experimentally determined geometric parameters of the virgin electrode medium. All of the electrode structures occupy a volume of dimensions $900 \times 135 \times 450$ μm^3 ($200 \times 30 \times 100$ voxels^3 at 4.5 μm per voxel resolution). A convention of dimensionless length, width, and height, X^*, Y^*, Z^*, respectively, are used throughout this paper, where each dimension is normalized relative to their respective total distance, i.e. $X^* = X/L$, $Y^* = Y/W$, and $Z^* = Z/H$.

2.2. Model equations

Pore-level transport models are developed to simulate the flow of electrolyte, the transport of ionic species (reactants and products), and transport of charge (electric current) through both the solid and liquid phases, as well as the electrochemical reactions at the electrode fiber surface. The governing equations for these phenomena are summarized in Table 2 and explained in detail in Qiu et al. [8]. The electrolyte is assumed to be Newtonian with a uniform viscosity and the flow is incompressible, driven by a constant pressure gradient in the Z-direction, and with a no slip
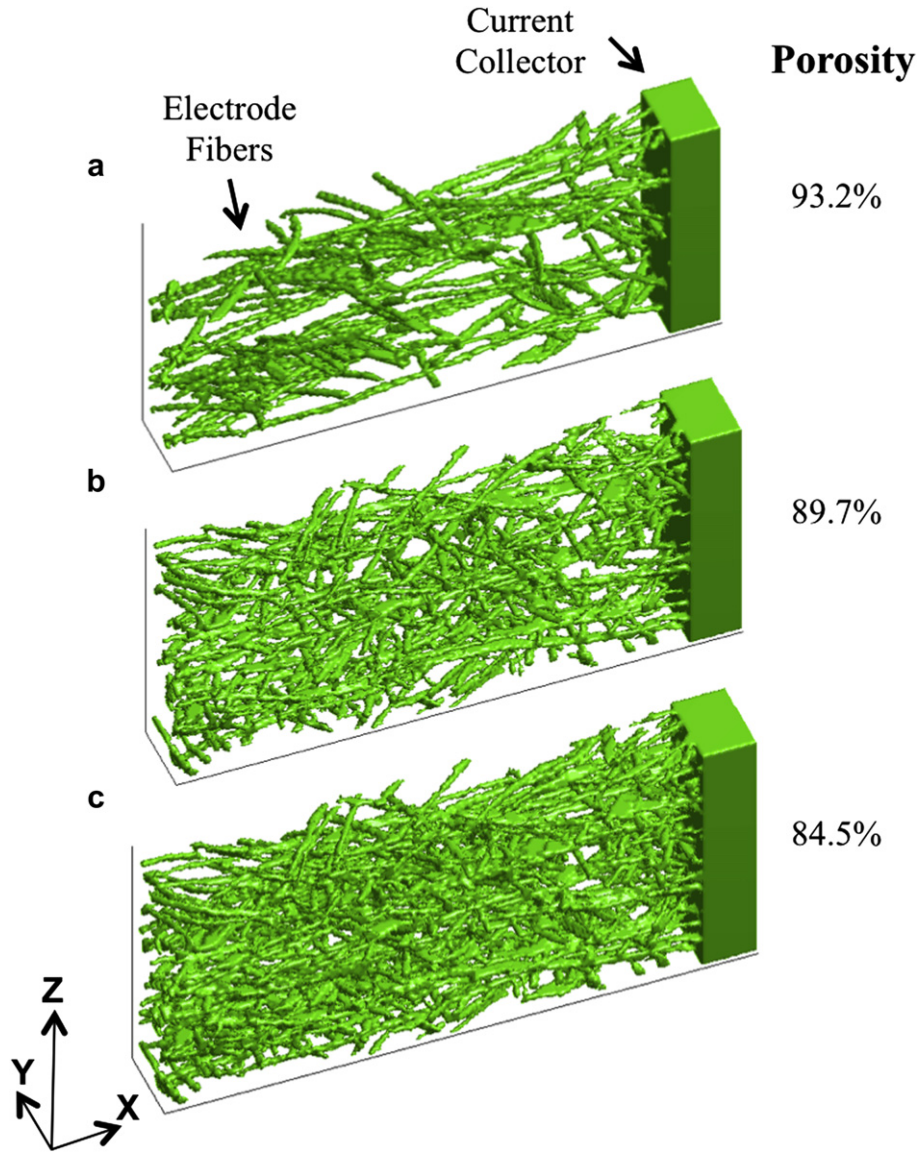
Fig. 2. 3D model geometries that are used in the pore-scale simulation. The fiber structures are digitally reconstructed from XCT imaging.

boundary condition at the fiber surface. The electrolyte is assumed to be dilute for all ionic species and the sulfuric acid completely dissociates into sulfate (SO_4^{2-}) and protons (H^+). The model parameters used in this study are given in Table 3.

In the present study, only the positive half cell is simulated. As such, only the transport of species $j \in \{V^{4+}, V^{5+}, H^+, H_2O\}$ is considered. It is convenient to define the inlet concentration of any species (C_j^{in}) in terms of the total vanadium concentration $(C^{0,+})$ and initial proton concentration $(C_{H^+}^{0,+})$ with respect to the state-of-charge (SOC) of the electrolyte using the following expressions:

$$
\begin{aligned}
SOC &= C_V/C^{0,+} \\
C_V^{in} &= C^{0,+} \cdot SOC \\
C_{IV}^{in} &= C^{0,+} \cdot (1 - SOC) \\
C_{H^+}^{in,+} &= C_{H^+}^{0,+} + C^{0,+} \cdot SOC
\end{aligned}
\tag{3}
$$

where the total vanadium and initial proton concentrations are given in Table 3. Unless otherwise stated, the SOC for all simulations is 50%.

A simplified treatment of the migration of H^+ and H_2O across the ion-exchange membrane is adopted for this work where the bulk generation and depletion of H^+ and H_2O in the half cell are accounted for by treating them as participants in the electrochemical reactions at the active surface with a stoichiometric rate of molar flux according to Eq. (2) [8]. The ion exchange membrane in this work is used as a grounded reference electrode, as seen in Fig. 1. It should also be noted that the migration term accounting for the effect of voltage gradients has a negligible effect in redox flow batteries [15] and therefore is ignored in this study.

Table 1
Geometrical properties of XCT-reconstructed carbon-felt electrode.

Structure		a.	b.	c.
Porosity	–	0.932 (0.9260[a])	0.897	0.845
Specific surface area	m^{-1}	29,600 (37,500[a])	47,700	69,700
Mean pore diameter	µm	197 (102.2 ± 8.27[a])	122	92.7
Mean fiber diameter	µm	17.1 (20.80 ± 6.53[b])	16.7	17.6

[a] Obtained from mercury intrusion porosimetry.
[b] Obtained from SEM imaging.

Table 2
Governing equations and boundary conditions [8].

Conservation equations		Boundary conditions
Fluid, electrolyte	$\nabla \cdot \mathbf{u} = 0, \quad \dfrac{\partial \mathbf{u}}{\partial t} + (\mathbf{u} \cdot \nabla)\mathbf{u} = -\dfrac{1}{\rho}\nabla p + \nu \nabla^2 \mathbf{u}$	$P\|_{z^*=0} = P^{\text{in}}, P\|_{z^*=1} = P^{\text{out}}$ $\left.\dfrac{\partial u}{\partial y}\right\|_{y^*=0} = \left.\dfrac{\partial u}{\partial y}\right\|_{y^*=1} = 0$ $\mathbf{u}\|_{\text{fiber}} = 0$
Species, electrolyte	$\dfrac{\partial C_j}{\partial t} + \mathbf{u}\cdot\nabla C_j = D_j\nabla^2 C_j + \nabla\cdot\left[\dfrac{z_j C_j D_j}{RT}\nabla\phi\right]$	$C_j\|_{z^*=0} = C_j^{\text{in}}$ $\left.\dfrac{\partial C_j}{\partial z}\right\|_{z^*=1} = \left.\dfrac{\partial C_j}{\partial y}\right\|_{y^*=0} = \left.\dfrac{\partial C_j}{\partial y}\right\|_{y^*=1} = 0$
Charge, electrode	$\nabla\cdot(\kappa_s\nabla\phi) = 0$	$-\kappa_s\left.\dfrac{\partial\phi}{\partial x}\right\|_{x^*=1} = J_{\text{ext}},$ $\kappa_s\left.\dfrac{\partial\phi}{\partial y}\right\|_{y^*=0}, \kappa_s\left.\dfrac{\partial\phi}{\partial y}\right\|_{y^*=1}, \kappa_s\left.\dfrac{\partial\phi}{\partial z}\right\|_{z^*=0}, \kappa_s\left.\dfrac{\partial\phi}{\partial z}\right\|_{z^*=1} = 0$ $\phi\|_{x^*=0} = 0$
Charge, electrolyte	$\nabla\cdot\left[\left(\dfrac{F^2}{RT}\sum z_j^2 D_j C_j\right)\nabla\phi + F\sum z_j D_j\nabla C_j\right] = 0$	$\kappa_e\left.\dfrac{\partial\phi}{\partial y}\right\|_{y^*=0}, \kappa_e\left.\dfrac{\partial\phi}{\partial y}\right\|_{y^*=1}, \kappa_e\left.\dfrac{\partial\phi}{\partial z}\right\|_{z^*=0}, \kappa_e\left.\dfrac{\partial\phi}{\partial z}\right\|_{z^*=1} = 0$
Electrochemistry (positive half cell) Reaction rate Overpotential	$\mathbf{N}_{\text{IV}}\cdot\hat{\mathbf{n}} = -\mathbf{N}_V\cdot\hat{\mathbf{n}} = k(C_{\text{IV}}^s)^{\alpha_c}(C_V^s)^{\alpha_a}\left[\exp\left(\dfrac{\alpha_a F\eta}{RT}\right) - \exp\left(-\dfrac{\alpha_c F\eta}{RT}\right)\right]$ $\eta = \varnothing_s - \varnothing_e - [E^0 + (RT/F)\ln(C_V/C_{\text{IV}})]$	

2.3. Numerical implementation

The numerical program is written in FORTRAN 90 using the Message Passing Interface (MPI) for parallel processing. Simulations are initiated by supplying the numerical model with the domain geometry, physical parameters, inlet velocity, SOC, and external current density at the current collectors. The lattice Boltzmann Method (LBM) [17] is then employed to solve for the flow field of the electrolyte inside the pore space of the electrode medium. A fully implicit 3D finite-volume method (FVM) [18] is then used to solve the coupled charge and species transport equations in the domain. A typical simulation of the XCT structures with a relative tolerance of 1×10^{-8} for all variables converges within 20 h using a 112-core cluster running on the NSF XSEDE system. Details of the numerical implementation are provided in Ref. [8] and a schematic of the multiphase simulation process is shown in Fig. 3.

The fluid velocity and pressure as calculated from LBM are in lattice units and are related to physical units through appropriate dimensionless quantities. As such, the physical fluid velocity is obtained by matching the Reynolds number (Re) in both lattice and physical units as follows:

$$\left(\frac{U_{\text{avg}} L_{\text{avg}}}{\nu}\right)_{\text{LBM units}} = \left(\frac{U_{\text{avg}} L_{\text{avg}}}{\nu}\right)_{\text{physical units}} \tag{4}$$

where the characteristic length scale, L_{avg}, is taken to be the average pore size based on the XCT data, the characteristic velocity, U_{avg}, is defined as the average velocity at the cell inlet ($Z^* = 0$), and the actual control volume size is the length scale ($\Delta x = 1$) in LBM units.

A prescribed pressure difference between the inlet and outlet is specified such that the desired flow rate is attained. Following a similar process, the applied pressure across the inlet and outlet of the flow cell can be converted from lattice units to physical units from the Euler number by using the following expression:

$$\left(\frac{\Delta P}{\rho U_{\text{avg}}^2}\right)_{\text{LBM units}} = \left(\frac{\Delta P}{\rho U_{\text{avg}}^2}\right)_{\text{physical units}} \tag{5}$$

3. Half-cell model verification

The half-cell configuration of the present study is a modification of the full-cell model that was previously validated against published experimental and simulated results [8]. Further verification

Table 3
Operating parameters used in the simulation.

Description	Symbol	Value	Units
Electrolyte density	ρ	1000	kg m^{-3}
Electrolyte viscosity	ν	1.0×10^{-6}	m^2 s^{-1}
Solid electrode conductivity	κ_s	1000[a]	S m^{-1}
Total vanadium concentration	$C^{0,+}$	2000[b]	mol m^{-3}
Initial proton concentration	$C_{H^+}^{0,+}$	4000[b]	mol m^{-3}
Initial water concentration	$C_{H_2O}^0$	4200[a]	mol m^{-3}
Anodic transfer coefficient	α_a	0.5[a]	–
Cathodic transfer coefficient	α_c	0.5[a]	–
Standard reaction rate constant	k	6.8×10^{-7} [16]	m s^{-1}
Equilibrium potential	E^0	0.991 [5]	V
Operating temperature	T	298	K
External current density	J_{ext}	400	A m^{-2}

Species	Symbol (C_j)	Charge (z_j)	Diffusivity [m^2 s^{-1}]
VO^{2+}	C_{IV}	+1	3.9×10^{-10} [13]
VO$_2^+$	C_V	+2	3.9×10^{-10} [13]
H$^+$	C_H^+	+1	9.312×10^{-9} [15]
H$_2$O	C_{H2O}	0	2.3×10^{-9} [13]
SO$_4^{2-}$	$C_{SO_4^{2-}}$	-2	2.2×10^{-10} [13]

[a] Estimated.
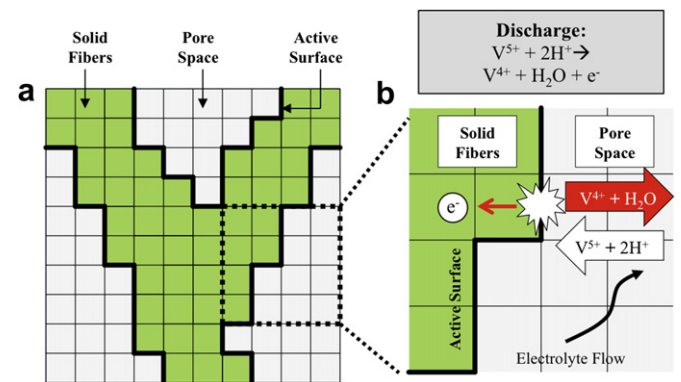[b] Based on vanadium solubility limit.

Fig. 3. Schematic of the pore-scale multiphase simulation geometry shown in a 2D plane. (a) Solid fibers (green) and pore spaces (grey) are assembled in a Cartesian lattice, with the interface between the two phases (bold black line) signifying the active surface where electrochemical reactions take place. (b) 4 × 4 subsection showing the electrochemical reaction occurring at an active surface for discharge of the positive half-cell, which is modeled using the Butler−Volmer equation. The fluid transport in the pore phase is solved using the LBM, while the species and charge transport is solved using the FVM. (For interpretation of the references to color in this figure legend, the reader is referred to the web version of this article.)

Table 4
Operating parameters (adopted from You et al. [15]) for the verification study.

Description	Symbol	Value	Units
Porosity	E	0.929	–
Specific surface area	A_e	16,200	m^{-1}
Half-cell width	L	0.003	m
Average velocity	u_{ave}	0.014	m s^{-1}
Initial vanadium concentration	C^0	1500	mol m^{-3}
Equilibrium potential	E^0	1.004	V
External current density	J_{ext}	−400	A m^{-2}

of the 3D half-cell model is performed in this section against the available half-cell simulation results that are presented for the 2D volumetric model of You et al. [15]. Table 4 summarizes the parameters that are adopted for this verification study. Note that a specially designed electrode structure is used [8] in order to preserve the geometric parameters used in the 2D volumetric model. Fig. 4(a) shows the averaged solid electrode potential as a function of the inlet SOC, while Fig. 4(b) shows the averaged surface overpotential along the X-direction for the positive half cell under galvanostatic charge of 400 A m^{-2}, which have average relative errors of 0.38% (3.9 mV) and 10.2% (0.41 mV), respectively. The slight discrepancies observed are most likely the contributions
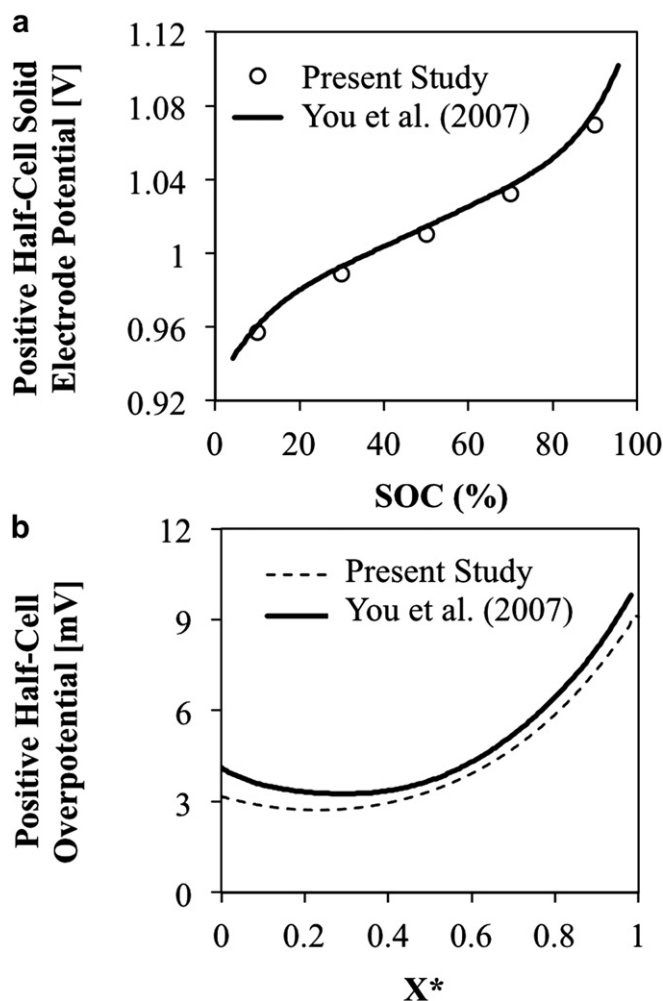
from the localized effects of fluid, species and charge transport that can only be captured using the pore-scale model.

4. Results and discussion

4.1. Effect of electrolyte flow rate

Flow rate is an important control parameter in the operation of the VRFB since low flow rates induce poor electrolytic circulation and yields stagnant regions (in terms of electrochemical activity) in the electrode while flow rates that are too high pose leakage risks and large pumping power requirements. In this study, flow rates that correspond to Re number of order 10^{-5} to 10 are simulated for the 93.2% porosity structure shown in Fig. 2(a) under galvanostatic discharge at 400 A m^{-2}, with a specified inlet SOC of 50%. For comparison, the Re's that are used in simulations [9,10,12,13,19] and experiments [20] range from 10^{-1}–1 and 10^{-2}–10, respectively.

The effect of flow rate on the total half-cell voltage and the associated pressure drop is shown in Fig. 5. The results indicate that performance improves with increasing flow rate. For low flow rate cases where Re ≤ 0.005, it is anticipated that mass transfer processes become diffusion-dominated, which result in large gradients in the concentration field. It also appears that for a flow rate of Re = 0.05, the gain in cell performance with increased flow rate becomes negligible under the prescribed operating conditions. Shah et al. and Al-Fetlawi et al. [9,10,12,13,19] also observed that marginal gains in output voltages decrease with increasing flow rate, although their study used a more limited range of flow rate. Our results indicate that there is a critical flow rate (approximately Re = 0.05 under these conditions) above which the output voltage saturates. As such, operating the VRFB at higher flow rates does not justify the exponentially increasing pumping power required.

Fig. 6 presents the local distributions of V^{5+} concentration normalized relative to its specified inlet value (herein referred to as concentration or electrolytic concentration) and surface current density for flow rates corresponding to Re = 0.05, 0.005, and 0.0005. From Fig. 6(1) it appears that the circulation of species improves with increasing flow rates. The large concentration and current density gradients in the diffusion-dominated cases can clearly be seen in Fig. 6(a1) and Fig. 6(a2), respectively. By contrast, more uniform distributions of concentration are observed from the convection-dominated mass transfer conditions in Fig. 6(c1), which indicate better circulation of the
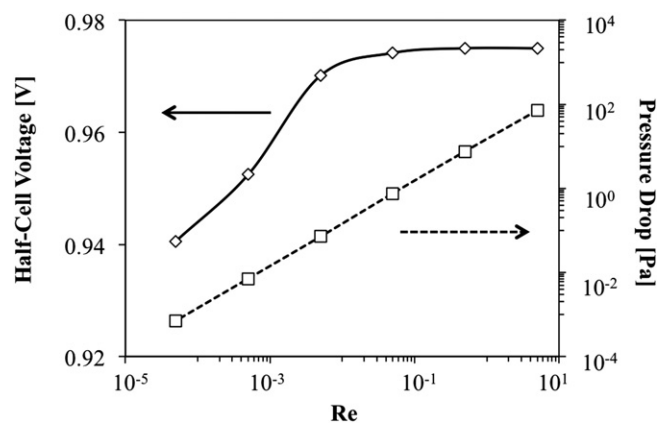

Fig. 4. Comparison of simulation results obtained using the 3D pore-scale model and the 2D volumetric model of You et al. [15] for the positive half cell under galvanostatic charge of 400 A m^{-2}. (a) Averaged solid electrode potential (average error = 0.38%) and (b) averaged X-direction surface overpotential (average error = 10.2%) at 50% SOC.

Fig. 5. Effect of flow rate on half-cell voltage and applied pressure drop. Simulations are performed on the 93.2% porosity half-cell electrode subject to galvanostatic discharge of 400 A m^{-2} with a specified inlet SOC of 50%.
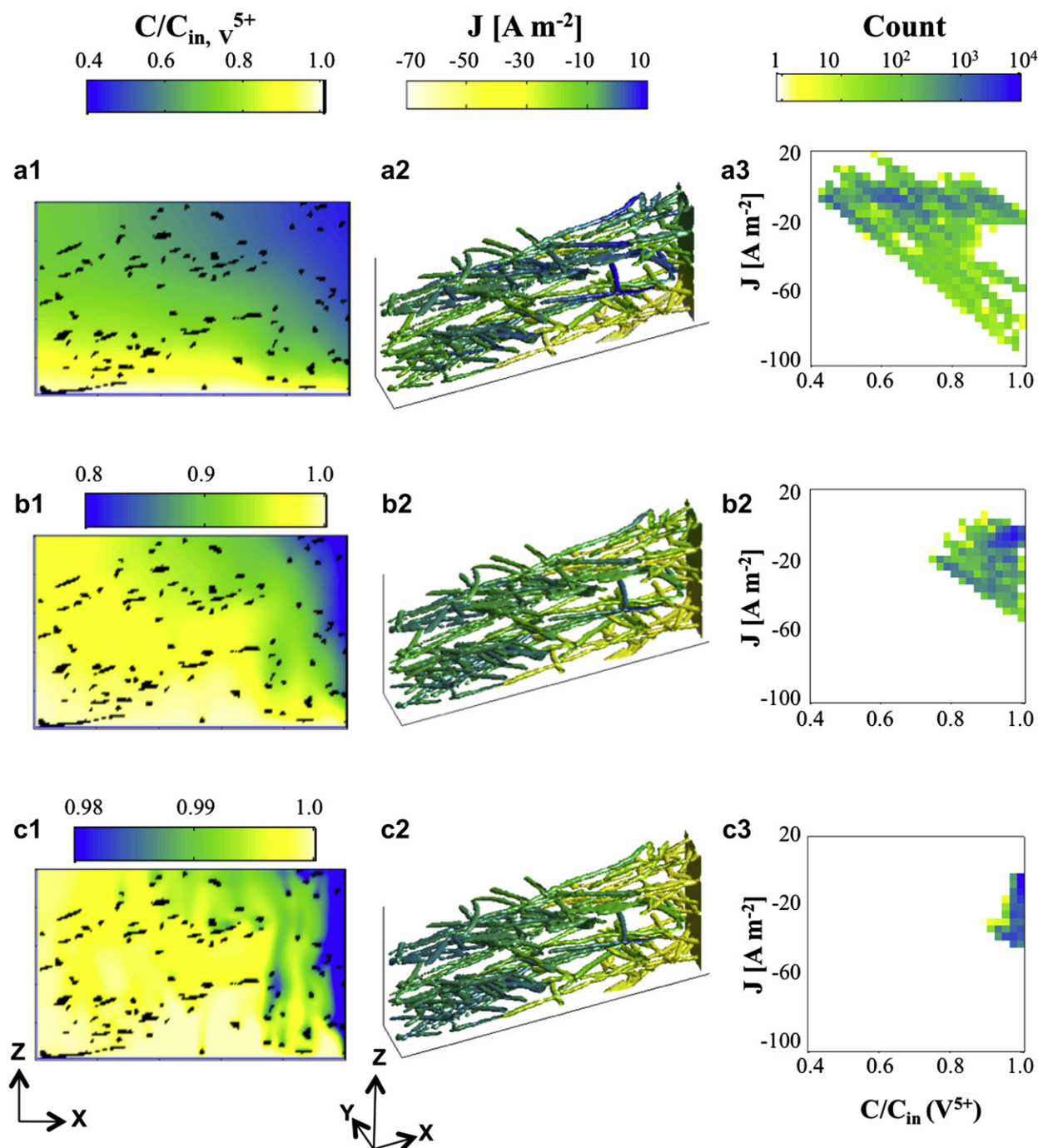
Fig. 6. Distribution of local transport properties shown on (1) a slice plot for the normalized V^{5+} concentration ($C/C_{in,V^{5+}}$) about the Y-midplane (note the different scale bars), (2) a surface plot of the current density (J) on the 3D electrode fibers, and (3) a scatter plot histogram of the corresponding J and $C/C_{in,V^{5+}}$ at every applicable control volume on the electrode structure (using 32 × 32 bins). Results are shown for different flow rates corresponding to Re's of (a) 0.0005, (b) 0.005, (c) 0.05. Simulations are performed on the 93.2% porosity half-cell electrode subject to galvanostatic discharge of 400 A m^{-2} with a specified inlet SOC of 50%.

reactants. In Fig. 6(3), the local concentration and current density at every discrete active surface on the electrode structure are collected in a scatter plot histogram. It can be seen that a larger scatter indicates more diffusion-dominated mass transfer conditions as a result of larger concentration and current density gradients. The lower diagonal slope seen in Fig. 6(a3), Fig. 6(b3), and to a lesser degree in Fig. 6(c3) suggests that the highest rates of reactions occur in regions with the highest electrolytic concentration.

Fig. 7 shows the spatial profiles of concentration, overpotential and current density in the X and Z-direction as well as their statistical distributions for all six simulated flow rates. Note that for flow rates of Re ≥ 0.05, the spatial and statistical distributions for all three parameters are nearly indistinguishable from each other, which indicates that (i) convection-dominated mass transfer conditions appears to exist at this flow rate and (ii) increasing the flow rate over the critical value ($\sim$Re = 0.05 under these operating conditions) will yield limited changes to the spatial distributions of
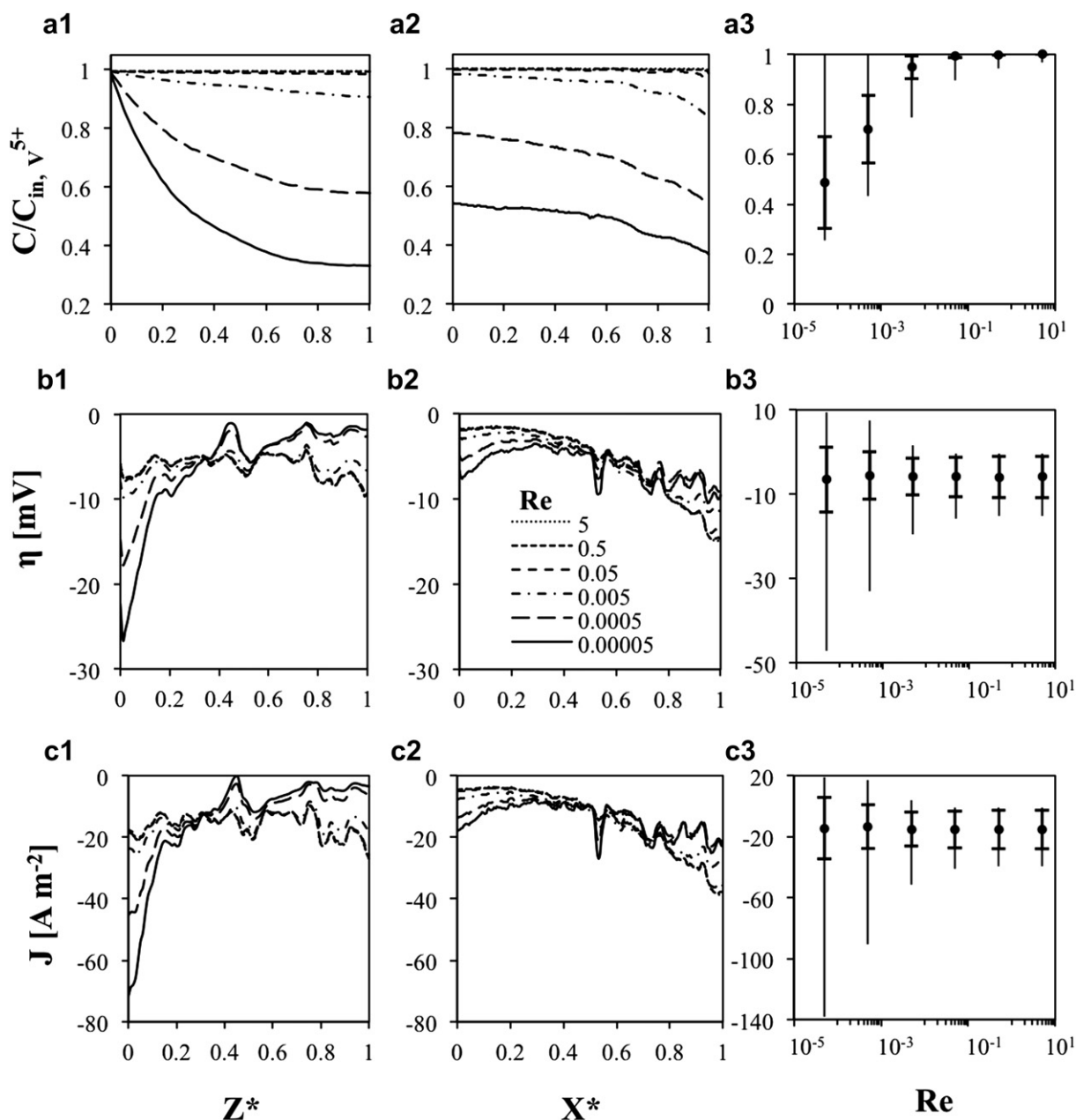
Fig. 7. Effects of flow rate on averaged distributions of (a) normalized V^{5+} concentration, (b) overpotential, and (c) current density along (1) the Z-direction and (2) the X-direction. Statistical information for each parameter in the entire domain is shown in (3), where the dots indicate the mean value, the capped bars indicate the variation to one standard deviation, and the uncapped lines indicate the minimum and maximum values. Simulations are performed on the 93.2% porosity half-cell electrode subject to galvanostatic discharge of 400 A m^{-2} with a specified inlet SOC of 50%.

concentration, overpotential and current density. For the diffusion-dominated cases, the high propensity for incoming reactants to oxidize near the inlet manifests itself in the steep gradients in all three parameters in the Z-direction, as seen in Fig. 7(1). For flow rates of Re $\geq$ 0.05, gradients in current density and overpotential are most pronounced in the direction perpendicular to the current collector, as seen in Fig. 7(b2) and Fig. 7(c2). It can be observed from Fig. 7(a2) that most reactions occur near the current collectors due to an increase of effective conductivity in the liquid electrolyte relative to the solid fibers as a result of the high porosity.

The statistical distributions shown in Fig. 7(3) are evaluated for every active surface in the entire 3D simulation geometry. Fig. 7(a3) shows that the average concentration decreases and that increasing concentration gradients are present at lower flow rates. Fig. 7(b3)

and Fig. 7(c3) suggests that: (i) the average overpotential and current densities remain constant for all flow rates, as required by Faraday's law; (ii) variations in these parameters increase with decreasing flow rate. These observations indicate that cell voltage will increase with increasing flow rates and abruptly saturate when convection-dominated mass transfer conditions are established (Re $\geq$ 0.05 under these operating conditions). Past this point, the concentration field approaches uniformity (to the value specified at the inlet), and so open circuit voltages saturate along with the overall cell voltages. It can be expected that with a larger simulation domain, concentration gradients will be larger, and so cell voltage will saturate at higher flow rates. It is important to note that for the diffusion-dominated cases, nonphysical positive values for over-potential and current densities are observed. These are purely

a mathematical artifact of the logarithmic term in the Nernst potential (which can be very large in areas of low concentration), and are found to occupy less than 1% of the entire total active surface.

4.2. Effect of electrode structure

The performance of VRFBs depends strongly on the morphology of the electrochemically active electrode. Only a few of the published computational studies have investigated the effects of electrode structures on cell performance [13–15]. These studies are based on volumetric models that use a homogenous domain characterized by macroscopic properties such as porosity and specific surface area to represent the porous electrode/electrolyte medium. Accordingly, these models reveal macroscopic trends such as decreasing porosity resulting in decreased permeability, bulk diffusion coefficients and increased bulk conductivity.

In this study, the pore-scale model is used to analyze the effect of the three electrode structures that are reconstructed from XCT images as shown in Fig. 2. Hereafter, it is implied that increasing porosity yields a decrease in surface area and vice versa. The tested structures are simulated with flow rates that correspond to Re numbers of order 10^{-5} to 10 under galvanostatic discharge at 400 A m^{-2} with a specified inlet SOC of 50%. Shown in Fig. 8 are the distributions of the half-cell voltage and corresponding applied pressure drop. The results show that higher voltages are delivered from the cell for denser electrodes at each flow rate. Additionally, the marginal trend in voltage with respect to flow rate observed for the 93.2% porosity structure from Fig. 5 is also extended to the less porous morphologies. Under these operating conditions, cell voltage is expected to saturate above a flow rate of Re = 0.05 for all three structures.

Fig. 9 shows the local distributions of normalized V^{5+} concentration and current density for the three electrode structures where flow rate is maintained on the order of Re = 0.05, under a galvanostatic discharge of 400 A m^{-2} and a specified inlet SOC of 50%. Note that for this study, flow rate is held constant such that the averaged velocity is on the order of Re = 0.05. The convection-dominated concentration field, characterized by small gradients, is shown in Fig. 9(1). From Fig. 9(2) it can be seen very clearly that decreased porosity will facilitate a more uniform current density distribution as a result of an increase in the fiber density and effective conductivity of the solid electrode. To clarify, electrodes with low effective conductivities result in higher reaction currents near the current collector, which occur in order to limit the amount of electronic current in the electrode. In the scatter plot histogram of Fig. 9(3) it can be concluded that for the same flow rate, decreased porosity will reduce both the range and gradients of concentration and current density.

The corresponding averaged spatial and statistical distribution of concentration, overpotential and current density for the three electrode structures are shown in Fig. 10. Greater concentration gradients are observed for lower porosity structures, as observed from the decrease in the mean, variation, and range in electrolytic concentration in Fig. 10(a). This observation can be explained by the fact that the concentration gradient is contingent on both the electrical discharge rate and the mass transfer conditions. Since the same current density is applied in all three cases, the reaction rate associated with the discharge rate should remain the same for all three electrode structures in accordance with Faraday's law. Increased porosity leads to increased effective diffusion coefficients and hydraulic permeability [13], resulting in better mass transfer conditions [15]. In addition, the decrease in surface area associated with porosity increase yields reduced
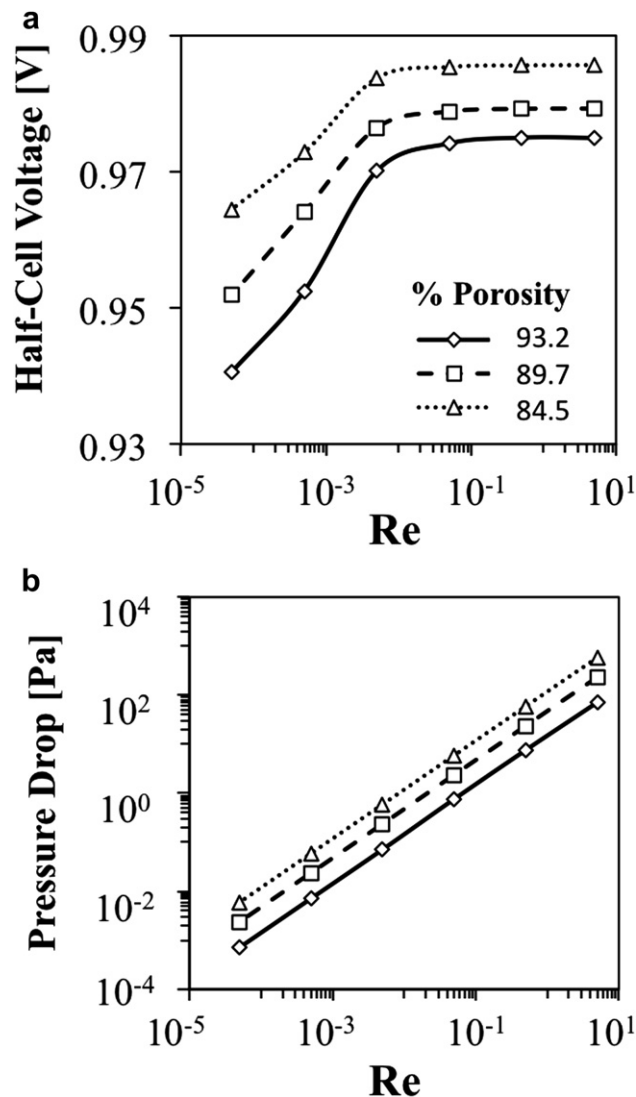
Fig. 8. Effect of porosity and flow rate on (a) half-cell voltage and (b) applied pressure drop. Simulations are performed for three different electrode structures subject to galvanostatic discharge of 400 A m^{-2} with a specified inlet SOC of 50%.

reaction, thereby decreasing concentration gradients. Our observation that lower porosity increases concentration gradients is in contradiction with Shah et al. [13] and in agreement with You et al. [15].

As the electrode structure decreases in porosity, more surface area is available for electrochemical reactions, and as a result lower current densities are required to yield the same bulk reaction rate as required by Faraday's law. Fig. 10(b) and Fig. 10(c) shows that the resulting overpotential and current density fields will be more uniform and have lower overall magnitudes. From Fig. 10(b2) and Fig. 10(c2), it can also be seen that the local polarity near the current collector is greater for higher porosity electrode morphologies. Since the effective conductivity of the solid electrode will increase with increasing fiber density, there will be less resistance in the solid phase, and so more reactions are expected to occur farther away from the current collector, as seen in Fig. 9(1). Additionally, the higher local current densities of the more porous structures is expected to contribute to higher local ohmic losses, which overall result in the lower half-cell voltages as observed in Fig. 8(a).
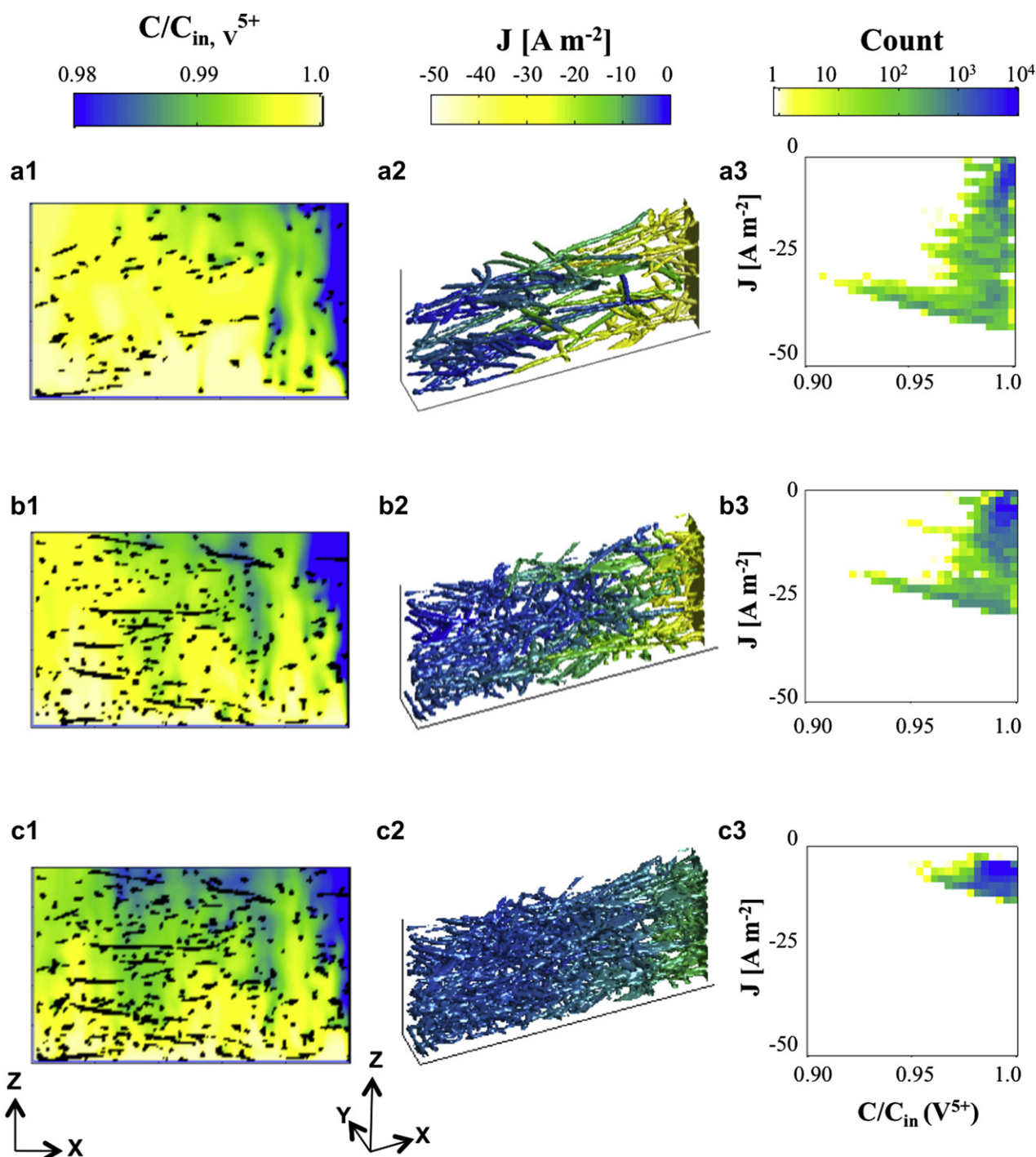
Fig. 9. Distribution of local transport properties shown on (1) a slice plot for the normalized V^{5+} concentration ($C/C_{in,V^{5+}}$) about the Y-midplane, (2) a surface plot of the current density (J) on the 3D electrode fibers, and (3) a scatter plot histogram of the corresponding J and $C/C_{in,V^{5+}}$ at every applicable control volume on the electrode structure (using 32×32 bins). Results are shown for different electrode structures corresponding to porosities of (a) 0.932, (b) 0.897, (c) 0.845 subject to flow rates of Re = 0.05, galvanostatic discharge of 400 A m^{-2} and specified inlet SOC of 50%.

4.3. Effect of SOC

The bulk electrolytic concentration will change continuously during the operation of the VRFB. This effect is studied by prescribing different SOCs at the inlet of the flow cell. The three electrode structures from Fig. 2 are subject to galvanostatic discharge of 400 A m^{-2} and a constant flow rate equivalent to Re = 0.5 for a range of SOCs specified at the inlet between 10% and 90%, so as to avoid the effect of oxygen and hydrogen evolution at higher polarizations which are not accounted for in the present model [15].

From Fig. 11(a) it is evident that the marginal gain in half-cell voltage is the same for all SOCs, and that higher output voltages are acquired at higher SOCs. The latter observation can be explained by the fact that higher SOCs lead to larger Nernst potentials, and so smaller localized liquid/solid voltage drops are
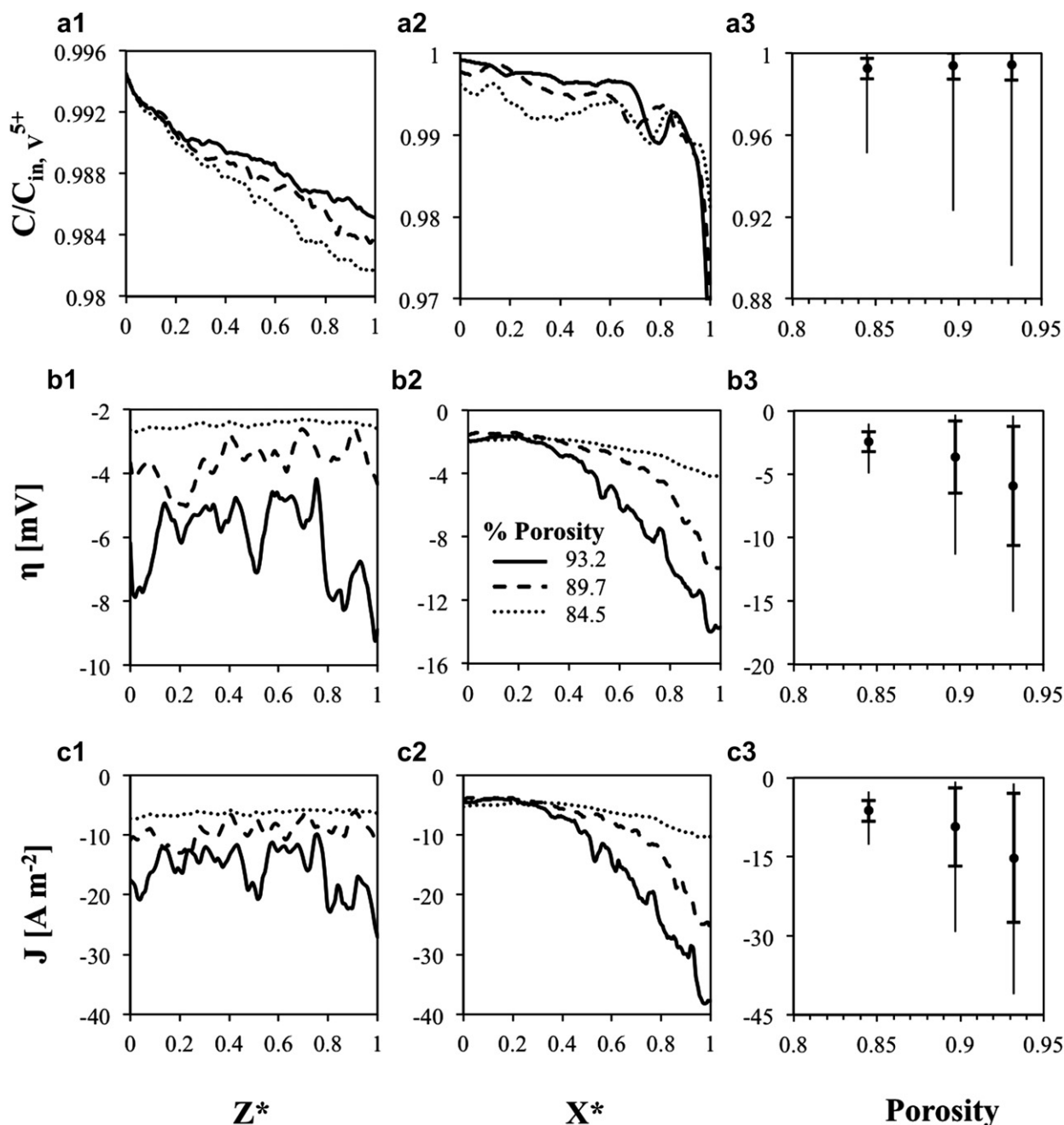
Fig. 10. Effects of porosity on averaged distributions of (a) normalized V^{5+} concentration, (b) overpotential, and (c) current density along (1) the Z-direction and (2) the X-direction. Statistical information for each parameter in the entire domain is shown in (3), where the dots indicate the mean value, the capped bars indicate the variation to one standard deviation, and the uncapped lines indicate the minimum and maximum values. Results are shown for different electrode structures corresponding to porosities of (a) 0.932, (b) 0.897, (c) 0.845 subject to flow rates of Re = 0.05, galvanostatic discharge of 400 A m^{-2} and specified inlet SOC of 50%.

sufficient to facilitate electrochemical reactions. Due to these changes in Nernst potentials, it is important to note that integrated average overpotential alone is not sufficient in predicting output voltages [21]. For instance, the symmetric overpotential profile about SOC = 50% [8,15] as seen in Fig. 11(b) may mislead some into believing that both high and low SOCs will result in higher output voltages.

In another study, a single electrode structure (the 93.2% porosity morphology in Fig. 2(a)) is subject to a range of flow rates (Re of order 10^{-5} to 10) as well as a range of SOCs (from 10% to 90%) under galvanostatic discharge of 400 A m^{-2}. From Fig. 12(a), it appears that higher SOCs result in higher overall voltages for all flow rates. Note that in the extreme case of low flow rate (Re $\leq$ 0.0005) and low SOC ($\sim$ 10%), a dramatic decrease in output voltage is observed. This observation can be explained by inspecting the averaged Z-direction concentration profile for three flow rates at 10% SOC. As shown in Fig. 12(b), below a flow rate of Re = 0.0005, a fuel starvation scenario exists, where the concentration gradient is so steep that all of the electrolytic species is consumed within the height (Z) of the flow cell. It can be seen that cell performance will vary strongly as electrolytic concentration changes during operation of the VRFB.
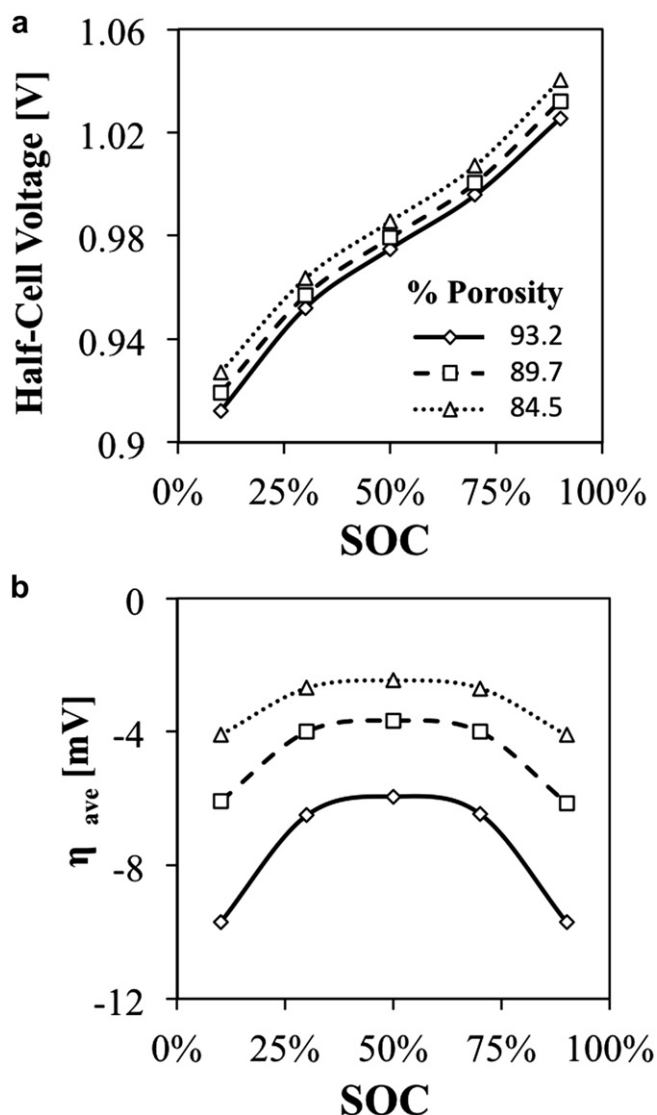
Fig. 11. Effects of porosity on (a) half-cell voltage and (b) overpotential as functions of specified inlet SOC under galvanostatic discharge of 400 A m^{-2} and constant flow rate of Re = 0.5.

Fig. 12. Effects of flow rate on (a) half-cell voltage for different specified inlet SOCs. (b) Normalized V^{5+} concentration in Z-direction for specified inlet SOC of 10%. Fuel starvation is observed for the Re = 0.0005 case. Simulation is performed for the 93.2% porosity structure under galvanostatic discharge 400 A m^{-2}.

5. Conclusion

An isothermal 3D pore-scale model [8] is used to investigate the effects of electrolyte flow rate, electrode morphology, and inlet SOC on performance characteristics of VRFBs. Virtual electrode structures are reconstructed from XCT data of a porous carbon felt material and analyzed in 3D using the pore-scale model. Localized, averaged and statistical distributions of concentration, overpotential and current density fields across the tested 3D electrode domains are determined to identify the key parameters affecting the electrolyte flow and utilization. The results show that overall cell voltage increases with increasing flow rate for the investigated electrode morphologies and SOCs as a result of decreasing concentration gradients. However, the marginal gain in cell voltage diminishes once the concentration field approaches uniformity at sufficiently high flow rates. It is also observed that cell performance improves for denser electrode structures with more active surface area, as a result of more uniform and lower absolute current density and overpotential fields. Finally, the simulations suggest that a significant detrim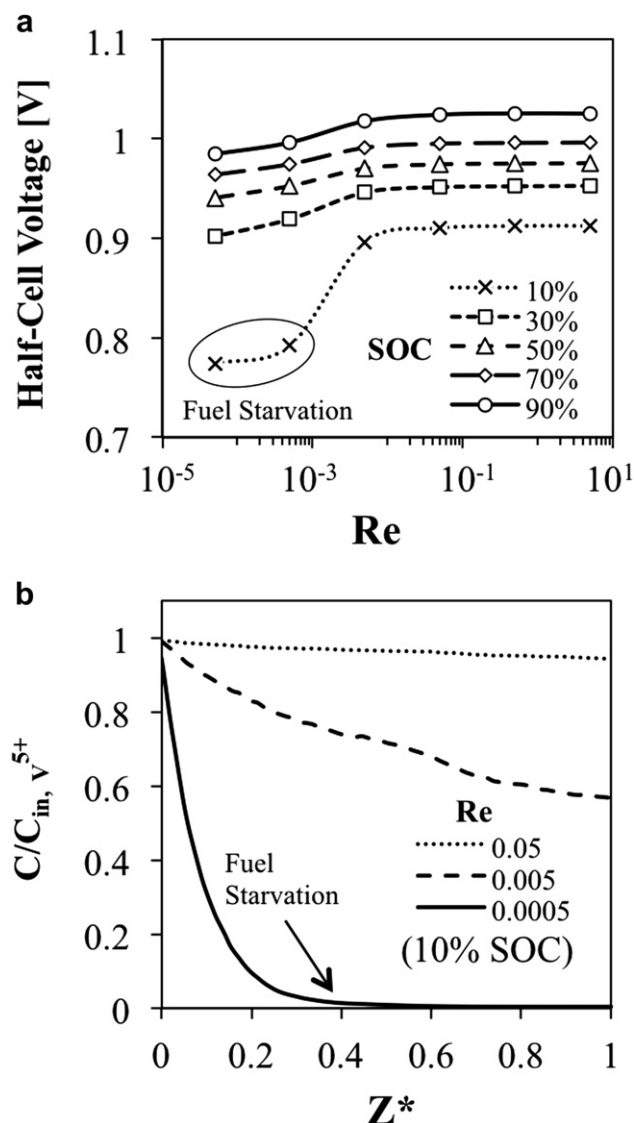ent to the performance of a VRFB occurs in the event of fuel starvation for low electrolytic concentrations and low flow rates.

References

[1] M. Skyllas-Kazacos, M. Rychcik, R. Robin, A.G. Fane, J. Electrochem. Soc. 133 (1986) 1057–1058.

[2] E. Sum, M. Rychcik, M. Skyllas-Kazacos, J. Power Sources 16 (1985) 85–95.
[3] E. Sum, M. Skyllas-Kazacos, J. Power Sources 15 (1985) 179–190.
[4] M. Pourbaix, Atlas of Electrochemical Equilibria in Aqueous Solutions, second ed., NACE International, Houston, 1974.
[5] D.R. Lide, CRC Handbook of Chemistry and Physics, 83rd ed., CRC Press, Boca Raton, FL, 2002.
[6] A. Weber, M. Mench, J. Meyers, P. Ross, J. Gostick, Q. Liu, J. Appl. Electrochem. 41 (2011) 1137–1164.
[7] M. Skyllas-Kazacos, M. Chakrabarti, S. Hajimolana, F. Mjalli, M. Saleem, J. Electrochem. Soc. 158 (2011) R55–R79.
[8] G. Qiu, A.S. Joshi, C.R. Dennison, K.W. Knehr, E.C. Kumbur, Y. Sun, Electrochim. Acta 64 (2012) 46–64.
[9] H. Al-Fetlawi, A.A. Shah, F.C. Walsh, Electrochim. Acta 55 (2009) 78–89.
[10] H. Al-Fetlawi, A.A. Shah, F.C. Walsh, Electrochim. Acta 55 (2010) 3192–3205.
[11] X. Ma, R. Balasubramaniam, R.S. Subramanian, Num. Heat Trans. A 35 (1999) 291–309.
[12] A.A. Shah, H. Al-Fetlawi, F.C. Walsh, Electrochim. Acta 55 (2009) 1125–1139.
[13] A.A. Shah, M.J. Watt-Smith, F.C. Walsh, Electrochim. Acta 53 (2008) 8087–8100.
[14] M. Vynnycky, Energy 36 (2010) 2242–2256.
[15] D. You, H. Zhang, J. Chen, Electrochim. Acta 54 (2009) 6827–6836.
[16] N.W. Yamamura, T.,T. Yano, Y. Shiokawa, J. Electrochem. Soc. 152 (2005) A830–A836.
[17] S. Chen, G.D. Doolen, Annu. Rev. Fluid Mech. 30 (1998) 329–364.
[18] S.V. Patankar, Numerical Heat Transfer and Fluid Flow, McGraw-Hill, 1980.
[19] A.A. Shah, R. Tangirala, R. Singh, R.G.A. Wills, F.C. Walsh, J. Electrochem. Soc. 158 (2011) A671–A677.
[20] E. Kjeang, B.T. Proctor, A.G. Brolo, D.A. Harrington, N. Djilali, D. Sinton, Electrochim. Acta 52 (2007) 4942–4946.
[21] K.W. Knehr, E.C. Kumbur, Electrochem. Commun. 13 (2011) 342–345.

Nomenclature

C: concentration [mol m^{-3}]
D: diffusivity [m^2 s^{-1}]
E^0: open circuit voltage [V]
F: Faraday's constant [C mol^{-1}]
H: total cell height [m]
$\boldsymbol{J}$: surface current density [A m^{-2}]

k: reaction rate constant [m s^{-1}]
L: average pore size [μm], total cell length [m]
$\hat{n}$: surface unit normal
$\boldsymbol{N}$: mole flux [mol m^{-2}]
P: fluid pressure [Pa]
R: universal gas constant [J mol^{-1} K^{-1}]
Re: Reynold's number
SOC: state of charge
T: operating temperature [K]
$\boldsymbol{u}$: velocity of the electrolyte flow [m s^{-1}]
W: total cell width [m]
X: component in the X direction [mm]
Y: component in the Y direction [mm]
Z: component in the Z direction [mm]

Greek

α: transfer coefficient
η: overpotential [V]
ϕ: potential [V]
κ: conductivity [S m^{-1}]
v: electrolyte kinematic viscosity [m^2 s^{-1}]
ρ: electrolyte density [kg m^{-3}]

Subscript

a: anodic reaction quantity
avg: average quantity
c: cathodic reaction quantity
ext: externally applied quantity, current collector quantity
e: liquid electrolyte property
j: species $C_j, j \in \{V(IV), V(V), H^+, H_2O, SO_4^{2-}\}$
s: solid fiber phase property

Superscript

$*$: normalized quantity
0: equilibrium or initial quantity
in: cell inlet value
s: surface property
$+$: positive half-cell quantity
$-$: negative half-cell quantity